Engineering Large In-Plane Tensile Strains in Ge Microdisks, Microrings and Racetrack Optical Cavities

R.W. Millar[a], K. Gallacher[a], J. Frigerio[b], A. Ballabio[b], A. Bashir[c], I. MacLaren[c], G. Isella[b] and D. J. Paul[a]

[a] School of Engineering, University of Glasgow, Rankine Building, Oakfield Avenue,Glasgow,G12 8LT, UK
[b] L-NESS, Politecnico di Milano, Via Anzani 42, 22100, Como, Italy
[c] School of Physics and Astronomy, University of Glasgow, Kelvin Building, Glasgow, G12 8QQ, UK

Highly strained Ge micro-cavities are demonstrated, with biaxial equivalent tensile strains > 2 % at the top surface, demonstrating photoluminescence up to the detector cut-off of 2.5 μm wavelength. Ge on Si micro-disk, rings, and racetrack structures are investigated, which have been undercut by wet etching techniques. The anisotropy of the wet etch in the Si leads to the realization of novel, partially suspended structures. The strain distributions in the different cavity structures are discussed and compared with regard to the in-plane uniformity, peak strain level, and effect of the strain distribution on the Ge band-structure.

Introduction

Since the demonstrations of electrically (1) and optically pumped (2) Ge lasers there has been renewed interest in Ge as an active photonics material in the near infra-red (NIR). The quasi-direct bandstructure, with the L valley only ~ 140 meV below the Γ-valley, allows for strong absorption at the direct band corresponding to a wavelength of ~1550 nm, allowing for efficient photodiodes (3), modulators (4), and single photon detectors (5), as well as intersubband devices in the MIR (6). The large density of states (DOS) in the L-valley, however, means that even with degenerate n-type doping, large carrier injection is required before the quasi-Fermi level moves into the Γ, and population inversion can occur. This in turn has lead to high free carrier losses from electrons, which significantly increase the cavity losses. More recently, GeSn alloys have been demonstrated to be direct bandgap, and lasing has been demonstrated at low temperatures (7). The L-valley DOS still means that, even when direct bandgap, significant injection is required to invert the Γ-valley. A solution to enhance the direct bandgap electron concentration in both material systems is to apply tensile strain (8), which moves the direct band to lower energies at a greater rate then the L-valley, thereby increasing the tail of the Fermi function into the direct band and increasing the carrier concentration. A cross-over to direct bandgap is predicted to be between 1.6 and 2 % biaxial tensile strain.

A number of techniques have been used to apply tensile strain to Ge. Mechanically stressed membranes were used in early work to demonstrate high strains up to 1.9 % (9)(10). Top down approaches have since been used, where the residual tensile strain in

Ge epilayers is locally amplified in suspended bridge structures, as the regions at either end constrict (11).

Silicon nitride stressors are of interest due to their prior use in CMOS technologies, and been used to show high levels of strains in Ge pillars (12), waveguides (13)-(15) and microdisk structures (16). Microdisks structures are interesting candidates for highly stressed Ge lasers, as their compact nature allows for significant stress transfer with a low footprint. Initial work demonstrated microdisks with single layer silicon nitride stressors with strains of ~1 % at the top plane (17). Subsequent work showed that the vertical distribution of strain, and hence the modal overlap with the gain region could be improved with a double bonding technique (18), which leads to a microdisk fully encased in silicon nitride. Furthermore, groups have used stiction to bond strained Ge disks to oxide layers (19), with the potential for subsequent deposition of high stress silicon nitride layers. While these works have addressed a number of the key issues, there are some inherent disadvantages, such as electrically contacting in future devices, which would potentially be challenging with the presence of a dielectric layer on the underside of the disk.

In this work, a number of Ge on Si cavity structures are investigated with single silicon nitride stressors. Ge microdisk, ring and racetrack structures are demonstrated, and comparisons are made between the in-plane strain distribution and the effect on the bandstructure. Photoluminescence measurements are taken along with Raman spectroscopy, and finite element measurements are used to investigate the strain distributions in regions of the cavities inaccessible by experiment.

Growth

380 nm thick Ge epi-layers were grown on (100) p-Si wafers by low-energy-plasma-enhanced-chemical-vapor-deposition (LEPECVD) at 500 $^{\circ}$C (20). The layer was degenerately doped with phosphorous to doping densities of 2.5e19 cm^{-3}. In order to avoid out diffusion and dopant clustering, no thermal anneals were carried out (21), and therefore there is negligible strain in the epi-layer from the thermal mismatch of Ge and Si; this was confirmed by both XRD and Raman spectroscopy. A downside of this requirement is that there is likely to be a large number of threading dislocations, which is detrimental to optical emission (22). In future, growth techniques such as limited area growth of Ge in SiO_2 trenches could be used to reduce threading dislocations to ~ 1e6 cm^{-2}, as threads can more easily glide and terminate at the edge of the trench.

Fabrication

A range of disk, ring and racetrack structures were patterned in Hydrogen silsesquioxane (HSQ) resist using a Vistec VB6 electron beam lithography tool. The structures were dry etched in an STS ICP tool using a mixed recipe, with SF_6 and C_4F_8. This etch has previously been shown to have extremely low damage for electrical (23)(24) and optical devices. The devices were subsequently wet etched in TMAH and IPA, which negligibly etched Ge. It was found that the anisotropy of the etch can allow the undercut profile to be engineered by controlling the orientation of the Ge mask.

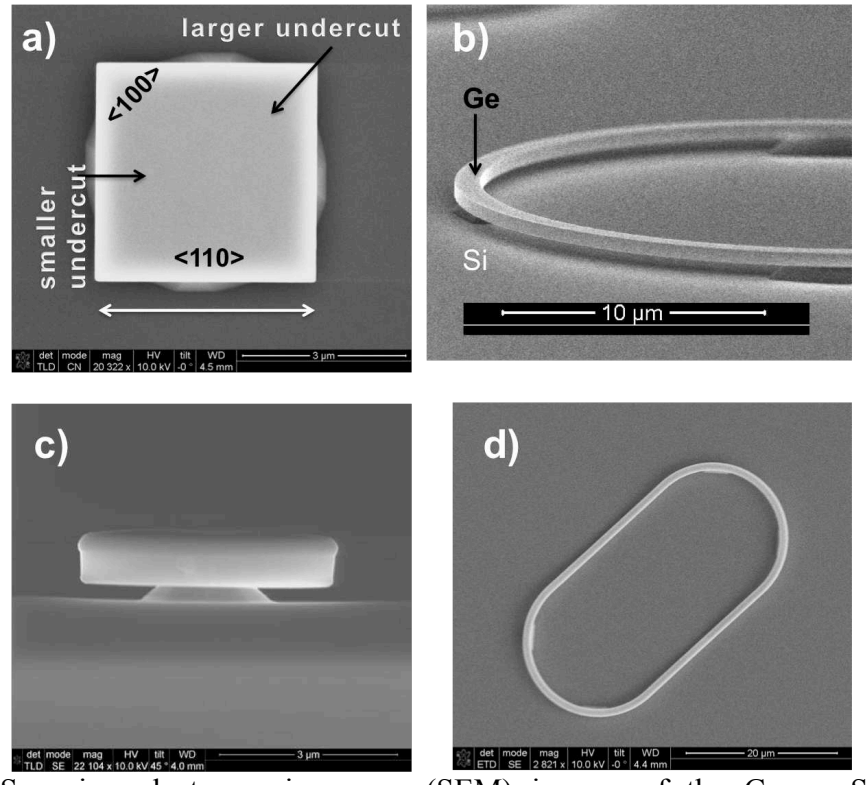

Figure 1. Scanning electron microscope (SEM) images of the Ge on Si undercut structures. a) A Ge square demonstrating larger undercut in the corners, parallel to the <100> directions. b) A Ge microring structure which has been fully undercut leaving support posts periodically around the ring. c) An undercut Ge microdisk coated in high stress silicon nitride. d) An undercut Ge racetrack structure, with supporting Si posts visible in the corners.

The undercutting profile of a Ge square is shown in Fig. 1a, and demonstrates that there is a larger undercut to masks lying in the <100> directions compared to the <110>. This is due to the fact that the {111} planes act as etch stop layers for TMAH etches, which is the plane undercutting the <110>. It was found that due to this anisotropy structures can be fully undercut in <100> directions, allowing for high strain transfer in these regions, as demonstrated in Fig. 1b.

A number of samples were fabricated containing arrays of disks and rings with diameters of 4, 5 and 6 µm; the rings had a constant waveguide width of 1.5 µm. Such arrays were used for photoluminescence with an unfocused yet collimated pump to ensure a low injection but to give a bright enough signal to give adequate signal to noise. In addition to the arrays, a number of independent features were patterned to allow characterization by Raman spectroscopy, including 10 and 30 µm diameter rings, and racetrack structures, shown in Fig. 1d.

Each sample was given a wet etch in TMAH, before the subsequent deposition of a high stress silicon nitride layer. The particular details of the wet-etch and the stressor layers will be given as the results are presented. For the silicon nitride deposition, an Oxford Instruments Systems 100 ICP tool is operated with increased platen power, giving films of ~ 2.4 GPa compressive stress. When this film relaxes, it transfers tensile strain into the underlying feature. Details of the stress measurement are given in (12).

Photoluminescence

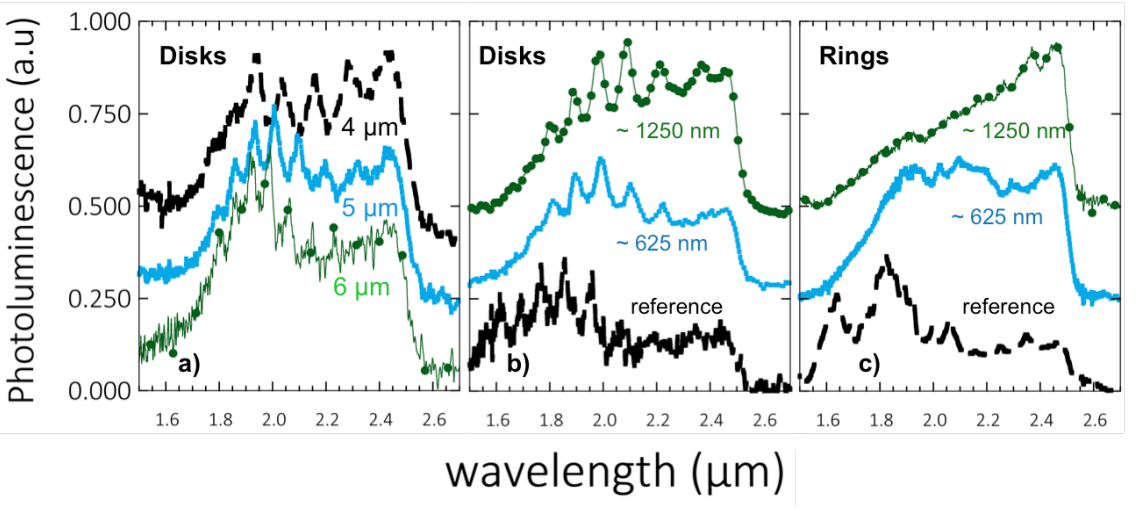

Figure 2. Photoluminescence (PL) measurements form various strained Ge microcavities. a) PL from 4, 5 and 6 µm diameter Ge disks with ~ 1300 nm undercuts and 2.45 GPa stressors. b) & c) PL from 4 µm disk and ring structures respectively, containing an unstrained reference and ~625 and 1250 nm undercut strained disks with 300 nm 2.37 GPa stressors.

Photoluminescence measurements were taken using a 532 nm Nd:YAG as the excitation source. The sample is illuminated through an aperture on a gold parabolic, which is also used to collect the sample emission. The emission is coupled into a Bruker Vertex 70 Fourier transform infrared spectroscopy (FTIR) system, and measured with a thermally cooled InGaAs detector with a cutoff at ~ 2.5 µm. Ambient blackbody spectra were subtracted from the measurement. The small additional heating caused by the pump causes a slight intensity increase in the blackbody emission, meaning that when the ambient is subtracted it leaves a tail towards the detector cutoff; this can be observed in Fig. 2b, particularly in the unstrained reference samples.

The emission from 4, 5, and 6 µm disks are shown in Fig. 2a. The disks are undercut by ~ 1300 nm and strained by a ~ 450 nm thick silicon nitride stressor with compressive stress of ~ 2.45 GPa. The emission from the disks exhibits Fabry-Perot like resonances from across the disk diameter. There is an observable redshift of the shortest wavelength resonance up to ~ 1.9 µm for the 4 µm disk. This is believed to indicate the position of the Γ to HH transition, which despite not being the smallest energy gap (which will be the Γ to LH), it is the shortest wavelength transition that will highly attenuate TE modes, due to the polarisation dependence of the interband transitions under biaxial strain (25). A Γ to HH transition at this wavelength would be consistent with approximately 2 % biaxial tensile strain, using deformation potentials from ref. (9). Further ring and disk structures were also examined with varying undercut (an unstrained undercut structure, and ~ 625 and 1250 nm undercuts with 300 nm thick 2.37 GPa stressors). The PL from disks and rings are shown in Fig. 2b and c. Interband transitions are more clearly observable with the absence of Fabry-Perot modes, and the constant peak near 1.8 µm across all ring samples is consistent with the L to HH transition. Emission clearly moves towards the cut-off detector at 2.5 µm, which is most likely from Γ to LH emission. This also

highlights the potential for Ge to be used a source for spectroscopy applications, moving in to the MIR.

Raman spectroscopy

Raman spectroscopy measurements were taken using a WITec Alpha RAS system. Similarly to the PL measurements, a 532 nm excitation source was used, which has a penetration depth of ~ 20 nm in unstrained Ge, therefore giving an accurate measurement of the strain at the top plane of the structures. The confocal system allows for excellent spatial resolutions and therefore the strained structures can be mapped, with the system recording a full Raman spectra at each pixel.

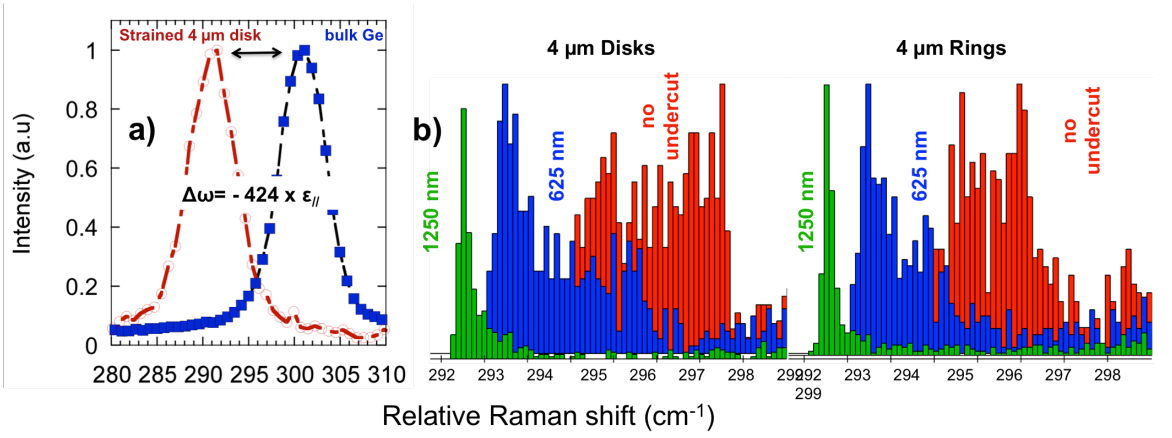

Figure 3. a) Raman spectra from a 4 µm disk with 2.45 GPa stressor and 1300 nm undercut showing 2.3 % biaxial equivalent tensile strain. b) Histograms from Raman maps of 4 µm disks and rings with 300 nm thick 2.37 GPa stressors with varying undercut. Each Raman spectra is fitted with a Lorentzian, before the peak position of the fits across the feature are binned into histograms.

Strain shift coefficients can be calculated using the phenomenological constants that describe the phonon frequency shifts with strain. The in-plane strain can be measured under the assumption that the strain in the z-direction is biaxially coupled to the in-plane strain. This leads to a biaxial equivalent strain shift coefficient of ~ 424 cm^{-1}, using the phenomenological constants reported (26). The highest strained disk structure (PL in Fig. 2a) demonstrates a large Raman shift of ~ –9.9 cm^{-1}, indicating a biaxial equivalent tensile strain of ~ 2.3 %, shown in Fig. 3a. It must be stressed that due to the self absorption of the Raman scattered pump only the top ~ 10 nm is probed by this measurements. This is in good agreement, however, with the PL measurements. Any discrepancy can be attributed to the vertical strain gradient. While both excitation sources are absorbed in the Ge surface, they probe different volumes of the structures. Carrier diffusion means that PL will originate from throughout the structures (27), whereas the Raman scattered signal at ~ 532 nm will be self-absorbed from any part of the disk lower than the top surface.

The effect of increasing undercut on otherwise identical structures (300 nm thick 2.37 GPa stressor layer) can be observed by the Raman histograms in Fig. 3b, demonstrating Raman shifts corresponding to ~ 2% for the fully undercut structures. As well as the increased peak strain with the increased undercut, there is greater in-plane uniformity,

which is advantageous for modal gain in potential Ge lasers. A number of larger ring structures were also examined by Raman spectroscopy. It might be intuitive to think that the constant waveguide size will lead to a comparable strain, but this was found not to be the case. Comparing 4 µm rings to 30 µm rings, with 1.5 µm waveguide widths and no undercut, it was found that the peak relative Raman shift reduced by > 1 cm^{-1} for the larger structure. The cause of this is explained in the following section.

Finite element modelling

A cross sectional TEM image was used to examine the curvature of the 4 µm with 450 nm 2.45 GPa stressor, which showed a vertical deflection of ~ 150 nm at the disk edge and was used to calibrate finite element models. This means that the strain distributions in regions of the disk that are inaccessible to experiment can be understood. The model demonstrated strain at the top plane of ~2.1 %, therefore in excellent agreement with experiment, and highlighting that the biaxial approximation for the Raman was valid. Using the same calibration for the various other cavities was found to provide excellent agreement with the experimental results.

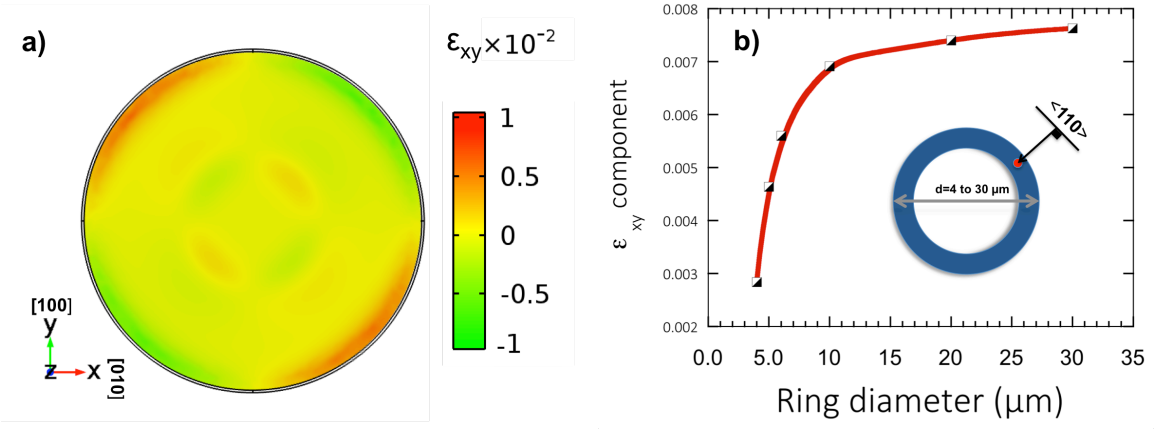

Figure 4. a) A 2D slice from a finite element model of the 4 µm disk shown in Fig. 2a, and 3a. The slice is 100 nm from the top surface, and shows the ε_{xy} shear strains. It can be observed that the strain component is at a minimum value when aligned to the <100> directions. b) The ε_{xy} shear strain component at the midpoint of the waveguide segment with a tangent in the <110> direction. The point probed is 100 nm from the top surface.

It was found that while large parts of the disk are biaxially strained there is a uniaxial stress component in the radial direction around the disk edge. When this is aligned to the <110> directions this induces a shear strain component (ε_{xy}), which causes a splitting of the normally degenerate L-valleys. This has been highlighted previously in straight waveguides (14)(15) but it has not previously been shown that such shear strains exist in strained microdisk structures. The presence of these shear strains are observable in Fig. 4a, which shows a 2D slice of a plane 100 nm down from the top surface of the Ge disk. The peak levels of ε_{xy} reach 0.5 % near the disk edge. This shear strain periodically changes between the peak value and zero (when aligned to the <100> directions) around the disk circumference.

The L-valley splitting is significant because it causes a reduction in the carrier concentration at the Γ, as the L-valley decreasing in energy effectively counteracting the application of biaxial tensile strain. It should therefore be properly included when

investigating the gain that is possible from such structures, which of course, this will depend on the modal overlap with the strain field. As an example of the effect; the addition of 0.5 % ε_{xy} shear strain to 2 % tensile biaxial strain, the carrier concentration at the Γ falls by 70 %. This was calculated using Fermi-Dirac integrals and does not include the strain induced modification of the effective masses of the Γ– and L-valleys.

A range of ring structures with no undercut were modeled in order to observe the effect of increasing the diameter on the strain distribution. Finite element models show that as the diameter is increased, the strain transverse to the waveguide segment dominates the tangential strain. This move away from a biaxial like strain distribution explains the reduced Raman shift observed for large diameter rings. As with the disks, when this transverse segment lies in the <110> directions it induces a ε_{xy} strain component that splits the L-valleys, however it is exacerbated the more the transverse strain dominates. As shown in Fig. 4b, the increased diameter increases the shear strain component.

In order to circumvent these shear strains, racetrack structures can be patterned with straight waveguide segments in the [100] direction. Conveniently, this direction is undercut more quickly therefore allowing a higher strain transfer. Raman spectroscopy was used to measure the strain in such segments, and it was found the peak strains of ~1.3 % could be achieved, in fully undercut 1 μm wide waveguide segments. It is worth noting that this suggests that smaller microdisk cavities are still likely to be preferable if large strain is required. Racetrack type structures hold other advantages, for instance with GeSn material systems, where moderate strain is required to overcome the residual compressive strain from growth on Ge virtual substrates. Undercuts would still allow increased strain transfer and modal confinement, however unlike with undercut disks, the remaining post structure lies directly underneath the waveguide segment which improves heat-syncing of the device, and gives scope to allow electrical injection. This is therefore a means of achieving a high Q cavity without the need for Bragg mirrors on a straight waveguide.

Conclusion

A range of micro-cavities were patterned and undercut using a wet etch in TMAH. The wet etch is anisotropic, and allows the creation of partially free standing structures for segments aligned to the <100> direction. The highest strained features were 4 μm Ge microdisks, which showed in-plane strains > 2% at the top surface, and emission up to the detector cut-off of ~2.5 μm, demonstrating that strained cavities can be engineered close to direct-bandgap single silicon nitride stressors. Finite element models reveal, however, that there is a periodic ε_{xy} shear strain component near the disk edge, which can reduce the carrier concentration at the Γ-valley, and should be taken into account when considering the potential gain available. Ring structures were used to observe interband transitions without Fabry-Perot resonances across the diameter. Similar strain profiles were found compared to the disks, however larger ring structures were found to have a reduced biaxial component to the strain, which exacerbates the ε_{xy} shear strain components. This therefore demonstrates that small disk structures are the best candidates for highly strained Ge resonators. An alternative proposed structure is a racetrack resonator, which can be fabricated with straight sections in the <100> directions to negate such shear strain issues, however the in-plane strain is reduced compared to disks. The

advantage brought by such structures is therefore the ability to have an undercut structure with high modal confinement, but the ability to have a Si post directly underneath the gain region, which aids with heat-syncing and gives the possibility for electrical contacting devices.

Acknowledgements

The authors would like to thank the staff of the James Watt Nanofabrication Centre for help with the fabrication. The work was funded by U.K. EPSRC (Project no. EP/N003225/1) and EC GEMINI (Project No. 613055).

References

1. R. E. Camacho-Aguilera et al., *Opt. Express*, **20**, 11316–20 (2012).
2. J. Liu et al., *Opt. Lett.*, **35**, 679–81 (2010).
3. J. Michel et al., *Nat. Photonics*, **4**, 527–534 (2010).
4. D.C.S. Dumas et al., *Opt Express,* **22**, 482–488 (2014).
5. R. E. Warburton et al., *IEEE Trans. Electron Devices*, **60**, 3807–3813 (2013).
6. K. Gallacher et al., *Appl. Phys. Lett.*, **108**, 091114 (2016).
7. S. Wirths et al., *Nat. Photonics*, **9**, 88–92 (2015).
8. D. J. Paul, *Electron. Lett.*, **45**, 582 (2009).
9. J. R. Sánchez-Pérez et al., *Proc. Natl. Acad. Sci. U. S. A.*, **108**, 18893–8 (2011).
10. C. Boztug et al., *Appl. Phys. Lett.*, **103**, 201114 (2013).
11. M. J Süess et al., *Nat Phot.*, **7**, 466–472 (2013).
12. R. W. Millar et al., *Opt. Express*, **23**, 18193 (2015).
13. M. de Kersauson et al., *Opt. Express*, **19**, 17925–34 (2011).
14. G. Capellini et al., Opt. Express, **22**, 102–109 (2014).
15. A. Ghrib et al., *Appl. Phys. Lett.*, **100**, 201104 (2012).
16. R. W. Millar et al., *Opt. Express*, **24**, 4365 (2016).
17. A. Ghrib et al., *Appl. Phys. Lett.*, **102**, 221112 (2013).
18. A. Ghrib et al., *Adv. Opt. Mater.*, **3**, 353–358 (2015).
19. D. Nam et al., *IEEE J. Sel. Topics Quantum Electron*, **65**, 1–6 (2013).
20. M. Kummer et al., *Mater. Sci. Eng. B-Solid State Mater. Adv. Technol.* **89**, 288 (2002).
21. R. Geiger et al., *Appl. Phys. Lett.*, **104**, 062106 (2014).
22. F. Pezzoli et al., *Appl. Phys. Lett.*, **108,** 262103 (2016).
23. M. M. Mirza et al., *J. Vac. Sci. Technol. B* **30**, 06FF02 (2012).
24. M. M. Mirza et al., *Nano Lett.* **14**, 6056 (2014).
25. D. S. Sukhdeo et al., *IEEE J. Sel. Top. Quantum Electron.*, **20**, 16–22 (2014).
26. D. J. Lockwood and J. F. Young, Eds., **273** (1991).
27. F. Pezzoli et al., *Phys. Rev. Appl.*, **1**, 044005 (2014).